# Aerosol microdroplets exhibit a stable pH gradient

Haoran Wei[a,b,c], Eric P. Vejerano[a,b,c,d], Weinan Leng[a,b,c], Qishen Huang[a,b,c], Marjorie R. Willner[a,b,c], Linsey C. Marr[a,b,c], and Peter J. Vikesland[a,b,c,1]

[a]Department of Civil and Environmental Engineering, Virginia Tech, Blacksburg, VA 24061; [b]Sustainable Nanotechnology Center, Virginia Tech Institute of Critical Technology and Applied Science, Blacksburg, VA 24061; [c]Center for the Environmental Implications of Nanotechnology, Duke University, Durham, NC 27708; and [d]Arnold School of Public Health, University of South Carolina, Columbia, SC 29208

Edited by Paul O. Wennberg, California Institute of Technology, Pasadena, CA, and approved May 16, 2018 (received for review November 23, 2017)

**Suspended aqueous aerosol droplets (<50 μm) are microreactors for many important atmospheric reactions. In droplets and other aquatic environments, pH is arguably the key parameter dictating chemical and biological processes. The nature of the droplet air/water interface has the potential to significantly alter droplet pH relative to bulk water. Historically, it has been challenging to measure the pH of individual droplets because of their inaccessibility to conventional pH probes. In this study, we scanned droplets containing 4-mercaptobenzoic acid–functionalized gold nanoparticle pH nanoprobes by 2D and 3D laser confocal Raman microscopy. Using surface-enhanced Raman scattering, we acquired the pH distribution inside approximately 20-μm-diameter phosphate-buffered aerosol droplets and found that the pH in the core of a droplet is higher than that of bulk solution by up to 3.6 pH units. This finding suggests the accumulation of protons at the air/water interface and is consistent with recent thermodynamic model results. The existence of this pH shift was corroborated by the observation that a catalytic reaction that occurs only under basic conditions (i.e., dimerization of 4-aminothiophenol to produce dimercaptoazobenzene) occurs within the high pH core of a droplet, but not in bulk solution. Our nanoparticle probe enables pH quantification through the cross-section of an aerosol droplet, revealing a spatial gradient that has implications for acid-base–catalyzed atmospheric chemistry.**

aerosol | droplet | pH | interface | SERS

At high relative humidity (RH), aerosols containing liquid water are ubiquitous and have a profound influence on local, regional, and global atmospheric processes (1, 2). For example, aerosol droplets in clouds influence the global radiation budget and the hydrologic cycle, which have uncertain feedback linked to factors driving climate change (3). At both local and global scales, sea spray and anthropogenic aerosols impact coastal and inland communities as well as climate through their capacity to absorb and scatter solar radiation and their role in cloud formation (4, 5). In addition, anthropogenic aerosols contribute to air quality problems in urban areas across the globe (6).

To quantify the impacts of these aerosols, we need to characterize their physical and chemical properties to understand how they influence in situ chemical reactions. In particular, the formation of organosulfates, acetals, esters/amides, and other compounds affects secondary organic aerosol production (7, 8). pH is arguably the key parameter defining droplet chemistry because of its central role dictating chemical speciation, partitioning, and reactivity (9, 10). pH is known to affect the reactive uptake of atmospheric gases, phase separation, and surface tension (11, 12). Nonetheless, it is analytically challenging to measure the pH of individual aerosol droplets due to the current dearth of tools that can detect pH within the confined droplet environment (13).

Water at the air/water interface exhibits different structure and hydrogen bond dynamics relative to bulk water, and these differences affect the pH of the near-surface region (14). Unfortunately, it is both experimentally and theoretically challenging to probe the air/water interface, and the acidity of that interface even more so (15). Electrophoretic mobility measurements of oil droplets and air bubbles in water indicate that this interface is negatively charged. The simplest explanation for this observation is the accumulation of hydroxide ($OH^-$) at the interface and the electrostatic repulsion of hydronium ($H_3O^+$). However, this conceptual model is inconsistent with surface sensitive experimental techniques, such as second harmonic generation and sum-frequency generation, that indicate that the interface is enriched in $H_3O^+$ (16). Molecular dynamics (17) and continuum solvent model (16) simulations further support the argument that $H_3O^+$ has greater affinity than $OH^-$ for the air/water interface, and that the water surface of an aerosol droplet is acidic (17).

Currently, aerosol pH values are typically calculated using thermodynamic models, such as E-AIM and ISORROPIA-II (10, 18, 19) that assume equilibrium between dissolved inorganic ions in the aqueous aerosol environment. However, these equilibrium models require measurement of the concentrations of multiple inorganic ions, along with temperature and RH, to estimate aerosol water content (20). ISORROPIA-II also neglects the impacts of organic ions, as well as particle phase and morphology. Furthermore, because aqueous aerosol particles are externally mixed, there is a significant need to obtain individual aerosol particle measurements in place of ensemble average or bulk measurements. Because aqueous aerosol particles can also be internally mixed, the ability to probe spatial heterogeneities within a single particle is also critical (13).

A number of spectroscopic and microscopic techniques, including electron microscopy, X-ray microscopy, fluorescence microscopy, single-particle aerosol mass spectroscopy, and Raman microscopy, have the potential for single-particle characterization (13). Raman spectroscopy in particular provides the capacity to differentiate the vibrational states of acids and their conjugate bases under ambient conditions that are not accessible with other techniques. Recently, Rindelaub et al. (21) used Raman spectroscopy to determine the pH of aerosol particles by tracking the ratio of the Raman bands of $SO_4^{2-}$ and $HSO_4^-$.

## Significance

Aerosols with high water content (aerosol droplets) are ubiquitous and play a significant role in atmospheric chemistry and meteorology. However, directly measuring the pH of an individual aerosol droplet remains challenging due to its inaccessibility to pH electrodes. In this study, nanometer-sized pH probes were dispersed in droplets to report pH via surface-enhanced Raman spectroscopy. The droplet core exhibits higher pH than the bulk solution, suggesting the presence of a stable pH gradient. This in situ technique extends pH characterization to confined water environments and deepens our understanding of aerosol chemistry and the air/water interface.

Author contributions: H.W., L.C.M., and P.J.V. designed research; H.W. and Q.H. performed research; H.W., E.P.V., W.L., and M.R.W. contributed new reagents/analytic tools; H.W., W.L., Q.H., L.C.M., and P.J.V. analyzed data; and H.W., L.C.M., and P.J.V. wrote the paper.

The authors declare no conflict of interest.

This article is a PNAS Direct Submission.



[1]To whom correspondence should be addressed. Email: pvikes@vt.edu.

This article contains supporting information online at www.pnas.org/lookup/suppl/doi:10.1073/pnas.1720488115/-/DCSupplemental.

Published online June 25, 2018.

Unfortunately, this approach was useful only in the highly acidic pH range near the $HSO_4^-/SO_4^{2-}$ $pK_a$ of 2. To extend this approach to a broader pH range (−1 to 10), Craig et al. (22) used a variety of acid-base pairs with different $pK_a$ values and determined the pH of individual particles at sizes down to 1 μm. Recently, surface-enhanced Raman spectroscopy (SERS) has been suggested as a technique to sensitively probe atmospheric aerosols (23, 24). SERS is an in situ method that can be used to probe water matrices, it exhibits extreme sensitivity (25), and it provides a highly stable signal.

We and others (26, 27) have shown that SERS provides the capacity to measure pH in confined aqueous environments. Using a plasmonic nanoparticle that has been surface-functionalized with a pH-sensitive amine or carboxylic acid it is possible to collect SERS spectra that change as a function of the local pH. Solution pH is then determined based on relative peak heights or changes in the band locations of specific vibrational modes. Here we used nano-sized pH probes to characterize the pH of individual phosphate-buffered aerosol droplets and found that they exhibited a stable pH gradient across a droplet that often exceeded three pH units. Phosphorous is an important, yet underappreciated, component of many aerosols (28–30). Phosphate is also useful as a buffer because, in contrast to ammonium, it exhibits minimal gas-particle partitioning. By combining the spatial resolution of a confocal Raman microscope with the inherent sensitivity of these probes, we were able to obtain 2D and 3D characterization of the pH distribution of μm-sized aerosol droplets under in situ conditions. The information acquired by this approach provides improved quantification of the pH of aerosol droplets.

## Results

**Principle of Droplet pH Detection by SERS.** Our experimental design is illustrated in Fig. 1. Aqueous microdroplets were generated from a 0.6 M phosphate buffer (PB) solution containing pH nanoprobes ($2 \times 10^{10}$ particles/mL) using a commercial atomizer (3076; TSI). Produced droplets were collected on a superhydrophobic surface prepared by drop-coating polydimethylsiloxane-treated silica nanoparticles onto a 0.22-μm polyvinylidene difluoride (PVDF) filter (Fig. 1*A*). The filter with the collected droplets was then placed in a humidity-controlled cell. Unless indicated otherwise, all the experiments were conducted at an RH of 97 ± 0.5%.

As illustrated in Fig. 1*A*, the pH nanoprobes consist of an acid–functionalized gold nanoparticle (AuNP) optical antenna, a thiolated polyethylene glycol (PEG) stabilizing layer, and the 4-mercaptobenzoic acid (4-MBA) pH indicator (26). 4-MBA is bifunctional, with a thiol group that covalently binds to the AuNP surface and a carboxylate group to detect pH changes. SERS spectra collected from nanoprobes in bulk solutions of 0.6 M PB with different initial pH values are shown in Fig. 1*B*. There are six characteristic Raman bands that change in intensity as the solution pH increases: (*i*) bands at 720 $cm^{-1}$ (out-of-plane ring hydrogen wagging), 850 $cm^{-1}$ ($COO^-$ bending), and 1,410 $cm^{-1}$ ($COO^-$ stretching) increase and (*ii*) bands at 700 $cm^{-1}$ (OCO bending), 810 $cm^{-1}$ (C-COOH stretching), and 1,710 $cm^{-1}$ (CO stretching) decrease (31). Simultaneously, the band at 1,590 $cm^{-1}$ (benzene ring breathing and axial deformation) shifts to a lower wavenumber (32). The other Raman bands in the spectrum are pH-insensitive, with the band at 1,080 $cm^{-1}$ (benzene ring breathing and axial deformation) the strongest. Because the pH-sensitive bands at approximately 1,410 and 1,710 $cm^{-1}$ shift slightly with a change in solution pH, the maxima of the two peaks irrespective of position were used for pH calculation. The ratios of the Raman bands at 1,710–1,080 $cm^{-1}$ ($I_{1710}/I_{1080}$) and 1,410–1,080 $cm^{-1}$ ($I_{1410}/I_{1080}$) were used to construct pH calibration curves (*SI Appendix*, Fig. S1).

**Collection and Raman Scanning of Microdroplets.** Following aerosolization, micrometer-sized aqueous droplets were observed across the filter, indicating successful droplet generation and collection (*SI Appendix*, Fig. S2). The droplets were highly spherical owing to the high contact angle of 157.3° imparted by the superhydrophobic

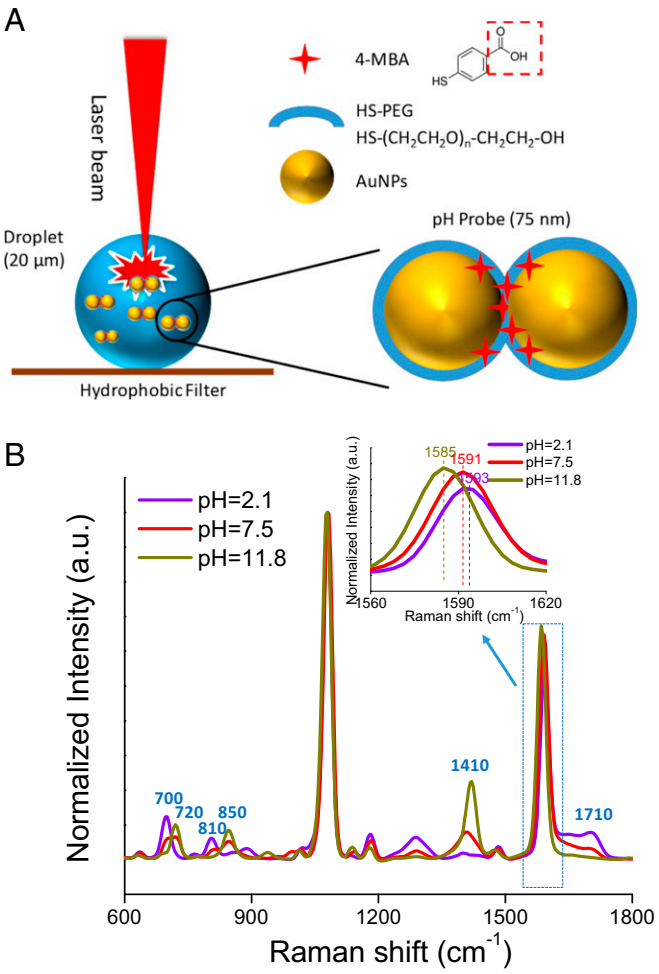


**Fig. 1.** pH detection of aerosol droplets using pH SERS nanoprobes. (*A*) Schematics illustrating SERS interrogation of aerosol droplets collected on a superhydrophobic PVDF filter and of SERS pH nanoprobes (not to scale). (*B*) SERS spectra of pH nanoprobes in bulk PB solutions (0.6 M) adjusted to different pH values.

substrate. Using ImageJ (33), we calculated an average droplet size of 19.5 ± 6.2 μm for 155 droplets collected on five separately prepared superhydrophobic filters, although droplets <10 μm were not enumerated due to their poor contrast against the substrate. Control experiments indicate that the pH nanoprobes did not significantly alter the droplet size distribution.

A key consideration for in situ droplet scanning is the stability of a droplet over the course of a measurement. We monitored droplet diameter as a function of time and, as shown in *SI Appendix*, Fig. S3, observed that it remained stable over a 44-min period due to our control of RH. The droplet diameter remained unchanged after an entire Raman scan using a 50× objective (*SI Appendix*, Fig. S4), indicating that the droplet was sufficiently stable for laser confocal Raman interrogation. In contrast, droplets scanned under supersaturated conditions grew over the course of 1 h (*SI Appendix*, Fig. S5).

Following the successful generation and collection of droplets, we scanned each droplet individually by confocal Raman microscopy using collection areas slightly larger than their respective diameters. As shown in *SI Appendix*, Fig. S6, the normal Raman spectrum of a droplet generated from a PB solution without added nanoprobes contains Raman bands for both PB (411, 539, 998, and 1,472 $cm^{-1}$) and the PVDF filter (802, 883, and 1,434 $cm^{-1}$). A Raman map made by tracking the band at 998 $cm^{-1}$ ($PO_4^{3-}$ stretch) is shown in *SI Appendix*, Fig. S2. The

ENVIRONMENTAL SCIENCES

area defined by the Raman signal is illustrated by the dotted circle. This circle is comparable to the droplet diameter determined from the optical image (27.0 vs. 27.6 μm), and the consistency of the signal across the droplet illustrates the uniform distribution of phosphate throughout the droplet. As shown in *SI Appendix*, Fig. S7, there is a linear relationship between the droplet diameter determined optically and that obtained by Raman imaging.

**The Core pH of a Droplet Is Higher than Bulk pH.** In the presence of the pH nanoprobes, the Raman signals arising from either the PB or the PVDF substrates were weak and were overwhelmed by the 4-MBA SERS signal (*SI Appendix*, Fig. S8). Nonetheless, SERS maps of droplets can be obtained by tracking the benzene ring breathing and axial deformation mode of 4-MBA at 1,080 $cm^{-1}$. As shown in Fig. 2*A*, the SERS maps of five different droplets exhibited variable patterns, indicating that the pH nanoprobes were not as uniformly distributed within each droplet as phosphate (*SI Appendix*, Fig. S2*D*).

We note that the droplet diameter determined from the 4-MBA SERS signal was consistently smaller than that obtained from the comparable optical images (Fig. 2*B* and *SI Appendix*, Fig. S9). This observation cannot be a result of the droplet being thicker in the middle and thinner at the edges, because the laser focal depth (3.2 μm) was much smaller than the droplet diameter. As shown in *SI Appendix*, Fig. S10, for a 20-μm droplet, the signals within a SERS map arise primarily from a cylindrical region with a width of 3.2 μm. In our system, the thickness of the laser excitation region should begin to decrease approximately 0.13 μm from the droplet edge (*SI Appendix*, Fig. S10). This distance is much smaller than the difference between the droplet diameters determined from the SERS signal and the optical image (*SI Appendix*, Fig. S9). The homogeneous signal distribution in the phosphate Raman map (*SI Appendix*, Fig. S2) further suggests only a minimal influence of changes in droplet thickness on the collected Raman signals. These results indicate that the PEG-coated AuNPs partition preferentially toward the droplet centroid and away from the comparatively hydrophobic air/water interface. It was recently suggested that polyvinylpyrrolidone (PVP)-coated silver nanoparticles accumulate preferentially at the air/water interface (34). We tested this hypothesis by synthesizing PVP-coated pH nanoprobes, but found that these nanoprobes partition preferentially toward the droplet centroid (*SI Appendix*, Fig. S11). We are currently developing nanoparticle-based pH probes that target the air/water interface.

A representative SERS spectrum collected from the center of a droplet is shown in Fig. 2*C*, along with the SERS spectrum for nanoprobes dispersed in bulk PB. All seven pH indicators suggest

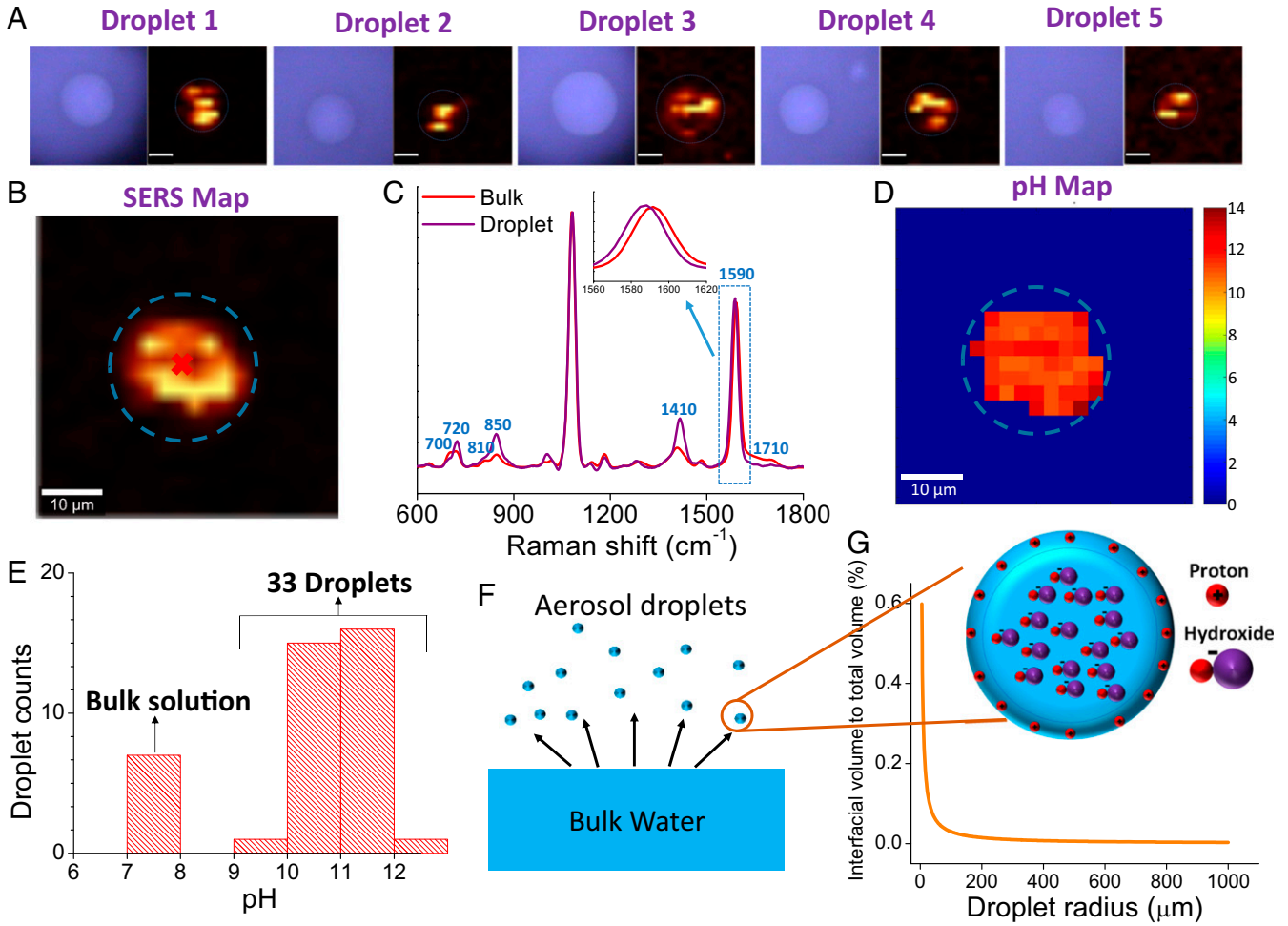


**Fig. 2.** Two-dimensional characterization of the pH inside aerosol droplets. (*A*) Optical images and Raman maps of droplets generated from 0.6 M PB + pH nanoprobes by tracking the 4-MBA Raman band at 1,080 $cm^{-1}$. Dashed circles indicate droplet edges. (Scale bar: 10 μm.) (*B*) Raman map of a droplet produced by tracking the 4-MBA Raman band at 1,080 $cm^{-1}$. (*C*) SERS spectra collected from bulk solution with pH 7.4 and a droplet generated from bulk solution. (*D*) pH map of the droplet shown in Fig. 3*B*. (*E*) pH at the centroid of 33 different droplets generated from bulk solutions with pH 7.4. (*F*) Schematic of the aerosol droplets generated from a bulk solution and the accumulation of protons at air/water interface in aerosol droplets. (*G*) Variation of interfacial volume to total volume of droplets as a function of droplet radius.

that the pH at the droplet centroid was much higher than the bulk solution (pH 7.4) from which the droplet was generated. The measured SERS signals were converted into pH values using the calibration curve (*SI Appendix*, Fig. S1) to produce 2D pH maps that reflect the measured pH distribution within the planar region bisecting the droplet. Interestingly, all the pixels exhibit pH values above the bulk solution pH of 7.4. This same result is illustrated in pH maps collected for 33 individual droplets in *SI Appendix*, Fig. S12. The measured average pH at the droplet centroid of 33 separate droplets was 11.0 ± 0.49 (Fig. 2*E*). This value is 3.6 pH units higher than the initial bulk pH. Control experiments in which the probe concentration was varied 0.5–2 times (our experimentally accessible range) indicate that the measured pH was not affected by the nanoprobe concentration (*SI Appendix*, Fig. S13). In addition, experiments using a range of initial pH values (2.1–10.7) indicate that the pH at the droplet centroid was consistently higher than the bulk pH (*SI Appendix*, Fig. S14).

An aerosol droplet should be considered a high-surface area object with a substantial portion of its volume in the near vicinity of the air/water interface (Fig. 2*F*). The ratio of interfacial volume to total volume ($Y$) as a function of droplet radius ($r$) can be mathematically expressed as

$$Y = 1 - \left(\frac{r-a}{r}\right)^3, \qquad [1]$$

where $a$ is the depth relative to the interface. As shown in Fig. 2*G*, $Y$ is essentially constant for a droplet radius of 100–1,000 μm. However, when the radius is decreased from 100 to 5 μm, $Y$ increases exponentially. In a 1,000-μm spherical water droplet ($V_{droplet} = 5.2 \times 10^{-10}$ m$^3$), approximately 0.003% of the total volume is within 10 nm of the surface. This percentage increases to 0.6% for a 10-μm droplet ($V_{droplet} = 5.2 \times 10^{-16}$ m$^3$). The large air/water interfacial volume could result in a large number of protons residing in this region, leaving a zone of higher pH in the droplet interior. We investigated the relationship between droplet diameter and the pH of the centroid and did not find any correlation (*SI Appendix*, Fig. S15). We attribute this fact to the limited range of droplet diameters (16–25 μm) investigated and the uncertainty of the height ($Z$) for the scans. As shown below, $Z$ has a significant influence on the measured pH.

**Three-Dimensional pH Distribution.** Two-dimensional scans of a microdroplet do not provide information about the pH of the interfacial region, because of two phenomena: (*i*) the pH nanoprobes partition preferentially toward the droplet centroid and (*ii*) at the droplet edge, the excitation laser is parallel to the air/water interface, and thus relatively few photons are backscattered by the interfacial region and collected by the detector. This second limitation can be partially overcome by 3D droplet scanning.

As illustrated schematically in *SI Appendix*, Fig. S16*A*, we systematically varied the $Z$ value of the objective both above and below the planar region bisecting a droplet. This approach was first tested by tracking the phosphate band at 998 cm$^{-1}$ for a droplet without nanoprobes. As shown in *SI Appendix*, Fig. S17, the maps became smaller as the $Z$ value increased, demonstrating the feasibility of 3D scanning. Subsequently, 3D scans of a droplet containing nanoprobes were collected. As the objective moved upward, the optical images of a droplet (22 μm) became increasingly blurry (*SI Appendix*, Fig. S16*B*). The SERS maps of the droplets exhibited different patterns due to the Brownian motion of the nanoprobes (*SI Appendix*, Fig. S16*C*). As shown in Fig. 3, the pH at the center of each map generally decreased as the objective moved from 0 to 20 μm. This phenomenon was replicated in a number of droplets (*SI Appendix*, Fig. S18).

As the objective moves upward, it gradually approaches the air/water interface. Therefore, the nanoprobes residing in the vicinity provide an increasingly larger contribution to the SERS signals that are collected, leading to the lower pH values. Although the interfacial depth is small (approximately 10 nm) relative to the focal depth (3.2 μm), the relative contribution of the interfacial region to the measured signal should be greater than that expected on a volume basis because of its different nature compared with the bulk (35, 36). Assuming that all the depleted protons from the noninterfacial volume migrate to the interfacial region, a high proton concentration within the interfacial region could induce the pH decrease illustrated in Fig. 3. In addition, when the focal point is above the top of the droplet, the ratio of the interfacial volume to the total excited volume within the droplet increases, which further increases the contribution of the interfacial region to the measured pH (*SI Appendix*, Fig. S19). This observation supports our speculation that the air/water interface accumulates protons.

To further support this conclusion, the objective was moved downward from 0 μm and Raman scans were conducted at each $Z$ value. As shown in *SI Appendix*, Fig. S16*D*, the contribution of the PVDF substrate to the collected SERS signal gradually increased when the objective was moved toward the droplet bottom. This phenomenon resulted in deteriorating contrast between the SERS signal and the background signal. Meanwhile, the pH values at the center of each Raman map decreased as the objective moved downward (Fig. 3). The observed differences in the slopes and the pH values at the extremes may reflect interactions between the droplet and the hydrophobic substrate. Nonetheless, in each case, the pH at the droplet core was substantially different than that at the droplet edge. Because of the large diffusion coefficients of $PO_4^{3-}$, $HPO_4^{2-}$, $H_2PO_4^-$, $Na^+$, and $K^+$ (0.82–1.96 × 10$^{-5}$ cm$^2$/s) (37), the potential for the observed pH gradient is unlikely to result from incomplete mixing of the salts in water; rather, the gradient is controlled by the air/water interface.

**Confirmation of Alkaline Droplet pH via Alkaline-Catalyzed Reactions.** To confirm the SERS results, we conducted experiments with a different pH indicator, 4-aminothiophenol (4-ATP). It was recently reported that two 4-ATP molecules colocated within a SERS hot spot dimerize to form dimercaptoazobenzene (DMAB) under alkaline conditions (Fig. 4) (38). Therefore, we expected that 4-ATP dimerization would be detectable in droplets because of the highly basic pH zone within the droplet core. To test this hypothesis, droplets containing 4-ATP-based nanoprobes were scanned. As shown in Fig. 4*B*, Raman bands at 1,138, 1,392, and 1,432 cm$^{-1}$ that reflect formation of an -*N*=*N*- linkage were detected in randomly selected droplets. Using the DMAB Raman band at 1,432 cm$^{-1}$, we constructed a SERS map of one droplet and observed consistently strong DMAB signals (Fig. 4*C*). In the control, no DMAB signals were observed within the SERS map of the bulk solution (Fig. 4*D*).

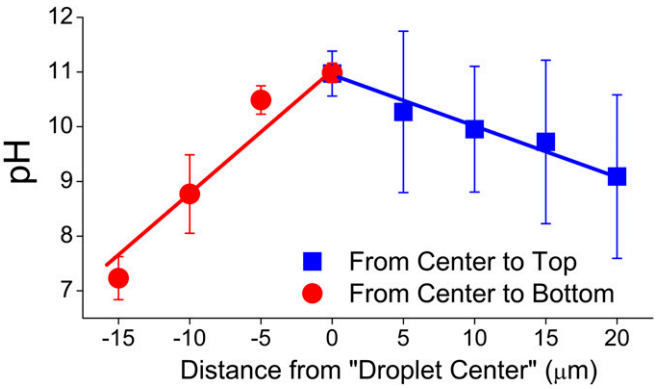


**Fig. 3.** Characterization of the pH inside aerosol droplets as a function of depth, $Z$. Each data point is the average of four parallel measurements with the error bars reflecting the SD of the four measurements. Each measurement is the average of four pixels within a 5 × 5 μm$^2$ area at the droplet center, with the error bars reflecting the SD of the four pixels.

The localized surface plasmon resonance of AuNPs can release heat through Landau damping and dramatically elevate the temperature (up to 465 K) in the nanoscale vicinity of NPs (39). Halas et al. (40) recently reported that plasmonic nanoparticles with high scattering cross-section can localize solar heat within a small volume at the solution surface when the nanoparticle concentration reaches the multiple scattering regime. To exclude the effect of localized heating on this dimerization reaction, bulk solution containing 4-ATP probes was heated in a boiling water bath for 15 min before Raman imaging. As shown in Fig. 4*E*, no signal for DMAB was observed, indicating that it is the pH, rather than the temperature, that accelerates the dimerization reaction in droplets. These alkaline catalytic reactions occurring in aerosol droplets generated from neutral bulk solution further indicate that the aerosol droplets are indeed basic.

## Discussion

Aqueous aerosols (droplets) are ubiquitous in the atmosphere and are acknowledged for their profound influence on many local-scale and global biogeochemical processes (1, 6, 41). In this study, we provide direct experimental evidence that the noninterfacial region of aerosol droplets is more basic than the phosphate-buffered bulk solution from which they were generated. We attribute this phenomenon to the preferential accumulation of protons within the interfacial region (Fig. 2*F*). While the underlying physics and chemistry dictating this behavior are at best only partially understood, two possible explanations are that hydronium preferentially orients such that positively charged protons point toward "bulk" water, with the electron-rich oxygen groups pointing outward toward the air. Such an orientation is consistent with the apparent negative surface charge of the interface. A second possibility is that localized disruption of the hydrogen-bond network in water stabilizes the Eigen cation structure ($H_9O_4^+$) of water at the interface, thereby leading to enhanced $H^+$ stability (17). In contrast to these studies, however, recent theoretical descriptions using the reactive and polarizable LEWIS model (42) have suggested that the air/water interface is enhanced in $OH^-$ (35, 36). The one overriding conclusion that can be derived from these and many other conflicting studies (43) is that the pH of the air/water interface is poorly understood at present. We hypothesize that these apparently divergent pH measurements may be a result of variations in the water chemistry inside the tested droplets. Such a hypothesis calls for laboratory measurements of droplet pH using advanced in situ techniques (44). Our ongoing studies are examining how aqueous and gas-phase chemistry affect the droplet pH gradient. We note that the droplets studied here are larger than many common aerosol particles due to the limitations of the instruments used to observe and scan submicron-sized particles. Single droplets of similar size, either levitated (45) or on surfaces (46, 47), have been used extensively as model targets and have provided useful insights with respect to atmospheric chemistry. However, we must be cautious when extrapolating our conclusions to smaller particles of different chemical compositions.

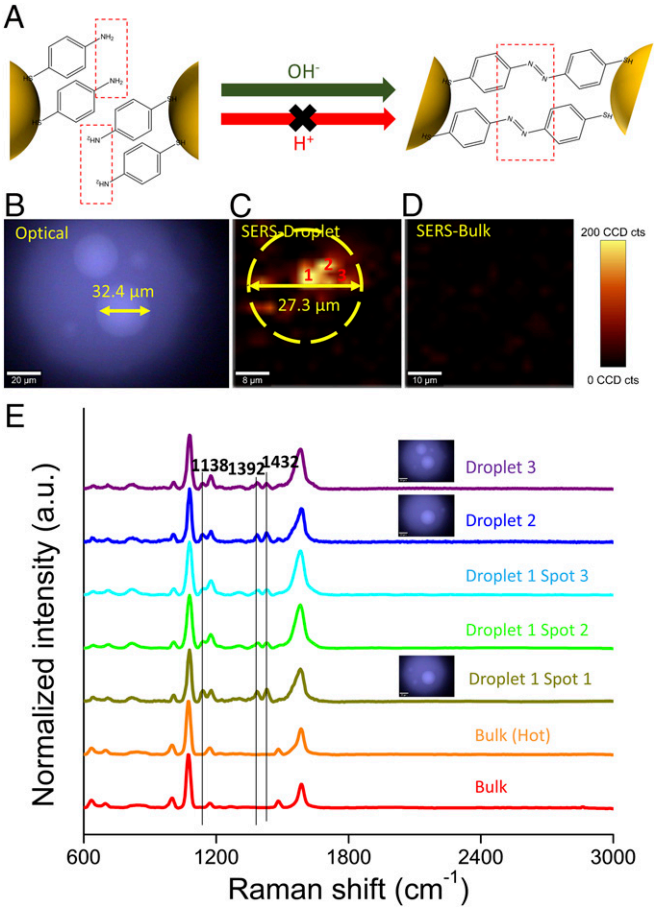


**Fig. 4.** Base catalyzed reaction occurs in droplets generated from neutral bulk solution. (*A*) Schematic for plasmon-catalyzed 4-ATP dimerization enhanced under alkaline conditions. (*B*) Optical image and SERS map of a droplet containing 0.6 M PB solution + 4-ATP–based nanoprobes. (*C*) SERS map of droplet containing 4-ATP–based probes constructed by tracking the DMAB band at 1,432 $cm^{-1}$. (*D*) SERS map of bulk solution constructed by tracking the DMAB band at 1,432 $cm^{-1}$. (*E*) SERS spectra of 4-ATP in different samples at room or elevated temperature.

It has been reported that the rates of many chemical reactions can be accelerated by up to several orders of magnitude in micrometer-sized droplets (microdroplets) generated by electrospray ionization (ESI) (48, 49). The reasons for such uncommon reaction rates are (although not unambiguously known) generally attributed to the unique air/water interfacial properties of the microdroplets, such as a high surface-to-volume ratio, altered pH, solvation, reagent molecule orientation in the interfacial region, microdroplet jet fission, and high electrostatic pressure (50). The latter two reasons are artifacts intrinsic to the ESI process. In this study, microdroplets were generated by an atomizer that excludes many of the aforementioned artifacts; nonetheless, our droplets still exhibit significantly accelerated reaction rates for an alkaline-catalyzed reaction. We argue that the pH gradient inside the microdroplet induced by the air/water interface is the primary cause of this phenomenon.

We have shown that a stable pH gradient exists within phosphate-buffered droplets. We observed a difference in pH of approximately four orders of magnitude between the starting bulk pH value and that measured at the droplet core. This difference reflects a decrease in the localized $[H^+]$ of approximately $10^{-7}$ M. While such proton gradients can be expected to be highly important for neutral to basic aerosols (e.g., sea spray) (51, 52), the implications of our findings to more acidic atmospheric aerosol droplets are unknown at present. Under acidic conditions, a difference of only approximately $10^{-7}$ M would make an insignificant contribution to the core pH if the exact same driving forces dictate pH gradient formation. We emphasize, however, that acidic aerosols characterized by the presence of ionizable sulfate and ammonium are considerably more complex than those examined herein, and our results illustrate the need for experiments under more acidic conditions. Our approach provides a useful technique for probing the pH of individual droplets, and the results showing differences in pH between a bulk solution and μm-scale droplets have important implications not only for atmospheric chemistry, but also for biology and other fields where chemical reactions inside droplets drive processes and reactions.

## Materials and Methods

Here we summarize our *Materials and Methods*. A more detailed discussion is available in the *SI Appendix*.

**Materials.** 4-MBA, 4-ATP, sodium citrate tribasic dehydrate ($Na_3Citrate{\cdot}2H_2O$), gold chloride trihydrate ($HAuCl_4{\cdot}3H_2O$), PVP (molecular weight 10,000), and 1 M PB were obtained from Sigma-Aldrich. Thiolated poly(ethylene) glycol (5 kDa) was purchased from Nanocs. AEROSILR202 (fumed silica treated with polydimethylsiloxane; average particle size 14 nm) was obtained from Evonik Industries. PVDF membrane filters (0.22 μm pore size, 13 mm diameter) were purchased from EMD Millipore.

**pH Nanoprobe Synthesis.** The synthesis of the SERS pH nanoprobes has been described previously (26) and is summarized in *SI Appendix*.

**Generation and Collection of Aerosol Droplets.** In these experiments, 2 mL of probe suspension was added to 3 mL of 1 M PB solution, followed by gentle mixing. Aerosol droplets were generated by aerosolizing this suspension with a commercial atomizer (3076; TSI) that was contained in a custom chamber designed to maintain RH (*SI Appendix*, Fig. S20). Aerosolized droplets were collected on a superhydrophobic filter placed approximately 1 cm away from the atomizer outlet. Following aerosolized droplet collection, the superhydrophobic filter was sealed in a flow cell connected to an automatic humidity controller (*SI Appendix*, Fig. S21) that maintained RH at 97.5%.

**Instrumentation.** Single aerosol droplets were scanned with a confocal Raman microscope using a 50× objective (WITec Alpha 500R) and a 785-nm laser. Raman scanning was enabled by a motorized scanning table with a lateral ($X$–$Y$) travel range of 150 × 100 mm and depth ($Z$) travel range of 30 mm with a minimum step size of 0.01 μm. Each pixel represents a single Raman spectrum collected with an integration time of 0.1 s. Bulk solution (0.6 mL) spectra were collected using a sealed quartz cell (Starna Cells).

**ACKNOWLEDGMENTS.** This research was supported by National Institutes of Health Director's New Innovator Award 1-DP2-A1112243 (to L.C.M.) and National Science Foundation Grant CBET-1705653 (to P.J.V. and L.C.M.). Additional support for H.W. and M.R.W. was provided by the Virginia Tech Graduate School through the Sustainable Nanotechnology Interdisciplinary Graduate Education Program.

1. Stevens B, Feingold G (2009) Untangling aerosol effects on clouds and precipitation in a buffered system. *Nature* 461:607–613.
2. von Schneidemesser E, et al. (2015) Chemistry and the linkages between air quality and climate change. *Chem Rev* 115:3856–3897.
3. Christensen MW, et al. (2017) Unveiling aerosol–cloud interactions, Part 1: Cloud contamination in satellite products enhances the aerosol indirect forcing estimate. *Atmos Chem Phys* 17:13151–13164.
4. Ault AP, et al. (2013) Raman microspectroscopy and vibrational sum frequency generation spectroscopy as probes of the bulk and surface compositions of size-resolved sea spray aerosol particles. *Phys Chem Chem Phys* 15:6206–6214.
5. Herrmann H, et al. (2015) Tropospheric aqueous-phase chemistry: Kinetics, mechanisms, and its coupling to a changing gas phase. *Chem Rev* 115:4259–4334.
6. Pöschl U, Shiraiwa M (2015) Multiphase chemistry at the atmosphere-biosphere interface influencing climate and public health in the Anthropocene. *Chem Rev* 115:4440–4475.
7. Lin YH, et al. (2012) Isoprene epoxydiols as precursors to secondary organic aerosol formation: Acid-catalyzed reactive uptake studies with authentic compounds. *Environ Sci Technol* 46:250–258.
8. Zhang H, et al. (2014) Secondary organic aerosol formation via 2-methyl-3-buten-2-ol photooxidation: Evidence of acid-catalyzed reactive uptake of epoxides. *Environ Sci Technol Lett* 1:242–247.
9. Schwarzenbach RP, Gschwend PM, Imboden DM (2005) *Environmental Organic Chemistry* (Wiley, Hoboken, NJ).
10. Weber RJ, Guo H, Russell AG, Nenes A (2016) High aerosol acidity despite declining atmospheric sulfate concentrations over the past 15 years. *Nat Geosci* 9:282–285.
11. Dallemagne MA, Huang XY, Eddingsaas NC (2016) Variation in pH of model secondary organic aerosol during liquid–liquid phase separation. *J Phys Chem A* 120: 2868–2876.
12. Boyer HC, Dutcher CS (2017) Atmospheric aqueous aerosol surface tensions: Isotherm-based modeling and biphasic microfluidic measurements. *J Phys Chem A* 121:4733–4742.
13. Ault AP, Axson JL (2017) Atmospheric aerosol chemistry: Spectroscopic and microscopic advances. *Anal Chem* 89:430–452.
14. Agmon N, et al. (2016) Protons and hydroxide ions in aqueous systems. *Chem Rev* 116: 7642–7672.
15. Saykally RJ (2013) Air/water interface: Two sides of the acid-base story. *Nat Chem* 5:82–84.
16. Duignan TT, Parsons DF, Ninham BW (2015) Hydronium and hydroxide at the air-water interface with a continuum solvent model. *Chem Phys Lett* 635:1–12.
17. Tse YLS, Chen C, Lindberg GE, Kumar R, Voth GA (2015) Propensity of hydrated excess protons and hydroxide anions for the air–water interface. *J Am Chem Soc* 137: 12610–12616.
18. Shi G, et al. (2017) pH of aerosols in a polluted atmosphere: Source contributions to highly acidic aerosol. *Environ Sci Technol* 51:4289–4296.
19. Murphy JG, et al. (2017) Observational constraints on particle acidity using measurements and modelling of particles and gases. *Faraday Discuss* 200:379–395.
20. Nguyen TKV, Zhang Q, Jimenez JL, Pike M, Carlton AG (2016) Liquid water: Ubiquitous contributor to aerosol mass. *Environ Sci Technol Lett* 3:257–263.
21. Rindelaub JD, et al. (2016) Direct measurement of pH in individual particles via Raman microspectroscopy and variation in acidity with relative humidity. *J Phys Chem A* 120: 911–917.
22. Craig RL, Nandy L, Axson JL, Dutcher CS, Ault AP (2017) Spectroscopic determination of aerosol pH from acid–base equilibria in inorganic, organic, and mixed systems. *J Phys Chem A* 121:5690–5699.
23. Craig RL, Bondy AL, Ault AP (2015) Surface-enhanced Raman spectroscopy enables observations of previously undetectable secondary organic aerosol components at the individual particle level. *Anal Chem* 87:7510–7514.
24. Fu Y, et al. (2017) Surface-enhanced Raman spectroscopy: A facile and rapid method for the chemical component study of individual atmospheric aerosol. *Environ Sci Technol* 51:6260–6267.
25. Etchegoin PG, Le Ru EC (2008) A perspective on single molecule SERS: Current status and future challenges. *Phys Chem Chem Phys* 10:6079–6089.
26. Wei H, Willner MR, Marr LC, Vikesland PJ (2016) Highly stable SERS pH nanoprobes produced by co-solvent controlled AuNP aggregation. *Analyst* 141:5159–5169.
27. Pallaoro A, Braun GB, Reich NO, Moskovits M (2010) Mapping local pH in live cells using encapsulated fluorescent SERS nanotags. *Small* 6:618–622.
28. Myriokefalitakis S, Nenes A, Baker AR, Mihalopoulos N, Kanakidou M (2016) Bioavailable atmospheric phosphorous supply to the global ocean: A 3-D global modeling study. *Biogeosciences* 13:6519–6543.
29. Anderson L, Faul K, Paytan A (2010) Phosphorus associations in aerosols: What can they tell us about P bioavailability? *Mar Chem* 120:44–56.
30. Longo AF, et al. (2014) P-NEXFS analysis of aerosol phosphorus delivered to the Mediterranean Sea. *Geophys Res Lett* 41:4043–4049.
31. Bishnoi SW, et al. (2006) All-optical nanoscale pH meter. *Nano Lett* 6:1687–1692.
32. Liu Y, Yuan H, Fales AM, Vo-Dinh T (2013) pH-sensing nanostar probe using surface-enhanced Raman scattering (SERS): Theoretical and experimental studies. *J Raman Spectrosc* 44:980–986.
33. Abràmoff MD, Magalhães PJ, Ram SJ (2004) Image processing with ImageJ. *Biophoton Int* 11:36–42.
34. Guo X, et al. (2016) Significant enrichment of engineered nanoparticles in water surface microlayer. *Environ Sci Technol Lett* 3:381–385.
35. Enami S, Hoffmann MR, Colussi AJ (2010) Proton availability at the air/water interface. *J Phys Chem Lett* 1:1599–1604.
36. Mishra H, et al. (2012) Brønsted basicity of the air-water interface. *Proc Natl Acad Sci USA* 109:18679–18683.
37. Haynes WM (2014) *CRC Handbook of Chemistry and Physics* (CRC Press, Boca Raton, FL).
38. Sun M, Huang Y, Xia L, Chen X, Xu H (2011) The pH-controlled plasmon-assisted surface photocatalysis reaction of 4-aminothiophenol to p, p′-dimercaptoazobenzene on Au, Ag, and Cu colloids. *J Phys Chem C* 115:9629–9636.
39. Neumann O, et al. (2013) Solar vapor generation enabled by nanoparticles. *ACS Nano* 7:42–49.
40. Hogan NJ, et al. (2014) Nanoparticles heat through light localization. *Nano Lett* 14: 4640–4645.
41. Seinfeld JH, Pandis SN (2016) *Atmospheric Chemistry and Physics: From Air Pollution to Climate Change* (Wiley, Hoboken, NJ).
42. Bai C, Herzfeld J (2016) Surface propensities of the self-ions of water. *ACS Cent Sci* 2: 225–231.
43. Björneholm O, et al. (2016) Water at interfaces. *Chem Rev* 116:7698–7726.
44. Marsh A, et al. (2017) Accurate representations of the physicochemical properties of atmospheric aerosols: When are laboratory measurements of value? *Faraday Discuss* 200:639–661.
45. Krieger UK, Marcolli C, Reid JP (2012) Exploring the complexity of aerosol particle properties and processes using single particle techniques. *Chem Soc Rev* 41:6631–6662.
46. Losey DJ, Parker RG, Freedman MA (2016) pH dependence of liquid-liquid phase separation in organic aerosol. *J Phys Chem Lett* 7:3861–3865.
47. You Y, et al. (2012) Images reveal that atmospheric particles can undergo liquid-liquid phase separations. *Proc Natl Acad Sci USA* 109:13188–13193.
48. Müller T, Badu-Tawiah A, Cooks RG (2012) Accelerated carbon-carbon bond-forming reactions in preparative electrospray. *Angew Chem Int Ed Engl* 51:11832–11835.
49. Bain RM, Pulliam CJ, Cooks RG (2015) Accelerated Hantzsch electrospray synthesis with temporal control of reaction intermediates. *Chem Sci* 6:397–401.
50. Banerjee S, Gnanamani E, Yan X, Zare RN (2017) Can all bulk-phase reactions be accelerated in microdroplets? *Analyst* 142:1399–1402.
51. Keene WC, et al. (1998) Aerosol pH in the marine boundary layer: A review and model evaluation. *J Aerosol Sci* 29:339–356.
52. Fridlind A, Jacobson M (2000) A study of gas-aerosol equilibrium and aerosol pH in the remote marine boundary layer during the First Aerosol Characterization Experiment (ACE 1). *J Geophys Res Atmos* 105:17325–17340.